JOURNAL OF AIRCRAFT
Vol. 43, No. 4, July–August 2006

Development and Experimental Validation of a Shipboard Helicopter On-Deck Maneuvering Simulation

Darren R. Linn* and Robert G. Langlois†
Carleton University, Ottawa, Ontario K1S 5B6, Canada

Routine shipboard helicopter operation on many classes of ships requires that helicopters be maneuvered and traversed along the ship deck using installed helicopter securing and handling equipment. This paper describes the derivation, implementation, and validation of a four-degrees-of-freedom mathematical model for predicting and analyzing the behavior of shipboard aircraft under the influence of external aircraft handling forces. The resulting model is suitable both for engineering analysis and training applications. The helicopter model includes the coupled dynamics of the aircraft, landing gear, and optionally steerable or castorable auxiliary wheel assembly. Detailed tire modeling addresses the transient development and release of tire deflection and cornering forces related to yawed and unyawed relaxation lengths as well as direct application of forces by the handling system. Verification and both qualitative and full-scale experimental validation of the model, performed using a number of simple maneuvers to validate specific aspects of the simulation, are discussed. It is shown that the resulting HeliMan simulation captures the underlying dynamics of the shipboard helicopter maneuvering process. Full-scale validation data show that in many cases the simulation is able to reproduce closely the measured data. The effect of tire side loading on longitudinal rolling resistance has been identified as a shortcoming of existing rolling tire models and the most probable cause for differences that exist between simulated and measured results in some validation cases.

Nomenclature

$\boldsymbol{A}$	=	vector representing the accelerations for the two bodies
$\boldsymbol{A}_C$	=	acceleration vector of the castor assembly
A_{ex}	=	equivalent cross-sectional area of the helicopter for the plane perpendicular to the x plane
A_{ey}	=	equivalent cross-sectional area of the helicopter for the plane perpendicular to the y plane
$\boldsymbol{A}_H$	=	acceleration vector of the main helicopter
a	=	Gauss elimination demonstration matrix
B	=	kinematic matrix
$\boldsymbol{C}$	=	vector representing the nonlinear components of the kinematic equations
C_B	=	coefficient of viscous damping at the castor pivot joint
C_{fix}	=	torsional damping coefficient used to fix the castor assembly
C_P	=	probe damping coefficient
C_{t_y}	=	tire lateral damping coefficient
C_{tz}	=	vertical tire force constant dependent on the tire type
$\boldsymbol{c}$	=	Gauss elimination demonstration vector
D	=	matrix used to isolate the unknown forces
D_{Ps}	=	small probe deflection stiffness transition displacement
$\boldsymbol{d}$	=	vector of tire deflections
d_{ss_y}	=	steady-state lateral tire deflection for a given slip angle
$\boldsymbol{E}$	=	elements of governing dynamic equation forcing vector
$\boldsymbol{F}$	=	vector containing the sum of generalized forces and moments
F_a	=	friction force between axle and wheel
$\boldsymbol{F}_B$	=	force vector acting on the joint pivot point B
$\boldsymbol{F}_c$	=	probe force vector caused by the probe damping
$\boldsymbol{F}_{\text{ct}_1}$	=	force vector acting on the first (left) castor tire
$\boldsymbol{F}_{\text{ct}_2}$	=	force vector acting on the second (right) castor tire
$\boldsymbol{F}_{\text{dx}}$	=	aerodynamic drag force vector acting in the helicopter longitudinal direction
$\boldsymbol{F}_{\text{dy}}$	=	aerodynamic drag force vector acting in the helicopter lateral direction
$\boldsymbol{F}_k$	=	vector containing known forces and moments
$\boldsymbol{F}_{\text{mlt}_1}$	=	force vector acting on the first (left) main left tire
$\boldsymbol{F}_{\text{mlt}_2}$	=	force vector acting on the second (right) main left tire
$\boldsymbol{F}_{\text{mrt}_1}$	=	force vector acting on the first (left) main right tire
$\boldsymbol{F}_{\text{mrt}_2}$	=	force vector acting on the second (right) main right tire
$\boldsymbol{F}_P$	=	force vector acting on the probe
F_{rr}	=	rolling resistance force
$\boldsymbol{F}_s$	=	probe force vector caused by the probe stiffness
F_{ss_y}	=	steady state lateral tire force for a given slip angle
$\boldsymbol{F}_t$	=	vector of tire forces
$\boldsymbol{F}_u$	=	vector containing unknown forces and moments
F_κ	=	force acting on the castor tires caused by the kingpin inclination angle
$\boldsymbol{F}^{\text{act}}$	=	actual force vector acting on the probe
$\boldsymbol{F}^{\text{mea}}$	=	measured force vector acting on the probe
h	=	height between castor pivot point and wheel pivoting arm perpendicular to the ground
I_C	=	mass moment of inertia of the castor assembly body
I_H	=	mass moment of inertia of the main helicopter body
K_{fix}	=	torsional stiffness used to fix the castor assembly
K_P	=	probe stiffness coefficient
K_{Ps}	=	small displacement probe stiffness coefficient
$\boldsymbol{K}_t$	=	vector of tire stiffnesses
k_h	=	radius of gyration of the helicopter
L_h	=	half-footprint length of tire
L_u	=	unyawed relaxation length
L_y	=	yawed relaxation length
l	=	distance perpendicular to the pivot axis to a plane perpendicular to the ground
M	=	mass matrix
M_B	=	sum of the reaction torques acting on the castor joint
m_C	=	mass of the castor assembly body

Received 8 October 2004; revision received 14 July 2005; accepted for publication 25 August 2005.

*Graduate Student, Department of Mechanical and Aerospace Engineering, 1125 Colonel By Drive.
†Associate Professor, Department of Mechanical and Aerospace Engineering, 1125 Colonel By Drive; rlangloi@mae.carleton.ca.

m_H = mass of the main helicopter body
N = cornering power of tire
n = polytropic exponent
P = instantaneous tire pressure
P_r = rated tire pressure
P_0 = tire inflation pressure at zero vertical load (gauge)
P_{oa} = tire inflation pressure at zero vertical load (absolute)
p_l = projected length
$\boldsymbol{q}$ = state vector
q_1 = helicopter X position in global coordinates
q_2 = helicopter Y position in global coordinates
q_3 = helicopter orientation in global coordinates
q_4 = castor assembly orientation relative to helicopter coordinate system
$\boldsymbol{R}_{B/C}$ = position vector of castor pivot point with respect to the castor center of mass
$\boldsymbol{R}_{B/H}$ = position vector of castor pivot point with respect to the helicopter center of mass
$\boldsymbol{R}_C$ = position vector of the castor assembly
$\boldsymbol{R}_{CPx/H}$ = position vector of the x center of pressure with respect to the helicopter center of mass
$\boldsymbol{R}_{CPy/H}$ = position vector of the y center of pressure with respect to the helicopter center of mass
$\boldsymbol{R}_{ct/C_1}$ = position vector of the first (left) castor tire with respect to the castor center of mass
$\boldsymbol{R}_{ct/C_2}$ = position vector of the second (right) castor tire with respect to the castor center of mass
$\boldsymbol{R}_H$ = position vector of the helicopter body
$\boldsymbol{R}_{mlt/H_1}$ = position vector of the first (left) main left tire with respect to the helicopter center of mass
$\boldsymbol{R}_{mlt/H_2}$ = position vector of the second (right) main left tire with respect to the helicopter center of mass
$\boldsymbol{R}_{mrt/H_1}$ = position vector of the first (left) main right tire with respect to the helicopter center of mass
$\boldsymbol{R}_{mrt/H_2}$ = position vector of the second (right) main right tire with respect to the helicopter center of mass
$\boldsymbol{R}_P$ = position vector of probe in global coordinates
$\boldsymbol{R}_{P/H}$ = position vector of probe with respect to the helicopter center of mass
$\boldsymbol{R}_{RSD}$ = position vector of RSD in global coordinates
$\boldsymbol{R}_{RSD/P}$ = probe deflection
$\boldsymbol{R}_t$ = displacement of wheel hub
r_a = radius of the tire axle
r_t = radius of tire
r_κ = absolute distance between castor pivot axis and the wheel axle
r_μ = radius of the kingpin
S_t = tire shape constant
T = transformation matrix
T_υ = torque acting on the castor joint caused by viscous damping
T_μ = torque acting on the castor joint caused by coulomb friction
$\boldsymbol{V}_C$ = velocity vector of castor assembly
$\boldsymbol{V}_H$ = velocity vector of the helicopter body
$\boldsymbol{V}_t$ = velocity of wheel hub
$\boldsymbol{V}_w$ = velocity vector of wind acting on the aircraft
$\boldsymbol{v}_{RSD}$ = vector of RSD velocities
w_t = width of tire
X_J = joystick x axis
$\boldsymbol{x}$ = Gauss elimination demonstration vector
Y_J = joystick y axis
α = instantaneous angle of castor wheel caused by the kingpin inclination
α_C = castor assembly angular acceleration
α_H = helicopter angular acceleration in global coordinates
β = exponential smoothing coefficient
γ_{lag} = lag coefficient for the rapid-securing-device (RSD) lateral float
Δd_y = intermediate lateral tire deflection caused by yawed or unyawed relaxation
ΔP = change in tire pressure
$\boldsymbol{\Delta r}_t$ = change in position of wheel hub
κ = kingpin inclination angle
μ = coefficient of friction between tires and the flight deck
μ_a = coefficient of friction between wheel and axle
μ_B = coefficient of friction at the castor pivot joint
μ_{rr} = coefficient of rolling resistance
ξ_c = direction of the probe force vector as a result of damping
ξ_s = direction of the probe force vector as a result of stiffness
τ = lateral tire type constant
ϕ = parameter based on the slip angle used to calculate the steady-state cornering force
φ = angle position error of the x axis strain gauge onto the probe
ψ = slip angle

Subscripts

x, y, z = x, y, and z components

Superscripts

c = castor assembly frame of reference
g = global frame of reference
h = helicopter frame of reference
i = initial value of variable
l = local frame of reference
m = manufacturer's helicopter frame of reference
max, min = a maximum or minimum value
t = tire frame of reference
$',''$ = adjusted value within a matrix or vector
$\cdot$ = first time derivative
$\cdot\cdot$ = second time derivative

I. Introduction

VARIOUS forms of equipment and associated procedures have been developed for shipboard helicopter securing and handling.[1] Systems vary in complexity, capability, and ease of use. One widely used system is the Indal Technologies, Inc. (ITI) Aircraft/Ship Integrated Secure and Transverse (ASIST) system illustrated in Fig. 1. ASIST provides integrated shipboard securing and handling using a ship-mounted rapid securing device (RSD) that secures an aircraft-mounted securing probe upon landing. On-deck handling is achieved by remotely applying independent longitudinal and lateral forces to the securing point, thereby allowing the aircraft to be straightened and traversed while remaining secured to the ship.

Various aspects of shipboard helicopter operation have been analyzed and reported in the open literature. Carignan et al.[2] have developed a physical simulation method to evaluate helicopter performance in hover above the flight deck. The effect of the air wake on rotor thrust and fuselage loads during hover has been addressed aerodynamically by Zan[3] and Lee and Zan.[4] McKillip et al.,[5] Lee et al.,[6] Aponso and Jewell,[7] and Keller and Smith[8] have also considered the effect the ship's air wake has on an approaching and hovering helicopter. Colwell[9] studied the effects of deck motion on pilot response using Fourier analysis and flight-test data. Bradley and Turner[10] have attempted to simulate the pilot hovering and landing on a ship flight deck. Numerous studies have addressed shipboard securing requirements including the quasi-static approaches of Wei et al.[11] and de Smit[12] and the transient dynamic approach of Langlois and coworkers.[13–18] Kang et al.,[19] He et al.,[20] and Xin and He[21] report development of a helicopter/ship dynamic interface time-domain simulation based on FLIGHTLAB software, where emphasis has been placed on the effects of the ship's airwake by incorporating computational fluid dynamics. Work by Keller and Smith[8] and Wall et al.[22] has addressed shipboard helicopter blade sailing.

The element that has not been addressed is the on-deck handling operations phase, where the aircraft is straightened and traversed

Fig. 1 ITI ASIST aircraft handling system (photo courtesy of ITI).

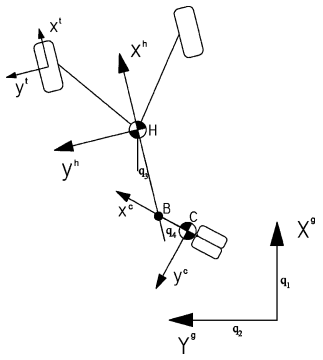

Fig. 2 Schematic of the dynamic helicopter model where H is the main helicopter body's center of mass and C is the castor assembly's center of mass.

along the deck and into the ship's hangar. This paper is intended to fill this void in existing capability. It describes the development and validation of a transient dynamic helicopter handling simulation. Considerable attention is focused on implementing a suitable tire model as tires form the primary interface between the helicopter and ship and are among the most important and complex force-producing elements involved.

Conventional aircraft and ground vehicle simulations assume negligible lateral tire deflections at low speed and assume no lag in the tire force generation when turning at higher speeds. During maneuvering, the helicopter tires roll at relatively low speed with relatively large deflections. This application requires using non-steady-state properties to model the relaxation length and cornering force generation of the tires.

Smiley and Horne[23] have compiled static and dynamic properties for modern aircraft tires and curve-fitted empirical formulas to the data.

A number of nonempirical tire models have also been developed. Two examples of analytical tire models can be found in Refs. 24 and 25. The analytical solutions use springs in spoke-like configurations to model the tire. Finite element representations have also been developed.[26–28]

Some aspects of taxiing fixed-wing aircraft have been found to be very similar to a maneuvering helicopter as both move with non-driven wheels. Aircraft taxiing was investigated by Hogg,[29] where the tire model of Smiley and Horne was used. Related work is presented in several additional references.[30–32] Sleeper and Smith present both experimental work[33] and a thorough simulation[34] testing parametric effects relevant for an airplane landing in a crosswind. Because of the high speeds, a time-lag tire model was found to have an insignificant effect. Equations of motion were derived using Lagrange's formulation with reaction forces undetermined at the castorable or steerable wheel pivot point. These forces were unnecessary because of the fixed castor wheel orientation.

II. Mathematical Model

The mathematical model has been broken into three parts: helicopter dynamics, simulation control, and simulation structure and solution.

A. Helicopter Dynamics Model

The generic helicopter on which the model is based is shown in Fig. 2. It consists of two bodies, representing the fuselage and the rotatable wheel assembly interconnected by a revolute joint located at point B, and three suspension stations each having either single or dual wheels. The geometry of the system is completely arbitrary with no implied assumptions of symmetry.

Figure 2 illustrates the four degrees of freedom included in the helicopter model, where the generalized coordinates q_i are the translational x position of the helicopter c.m., the translational y position of the helicopter c.m., the orientation of the helicopter, and the orientation of the optionally castorable wheel assembly relative to the helicopter body.

1. *Equations of Motion*

The core governing kinematic and dynamic equations for the helicopter model are developed to allow the extraction of joint reaction forces at the castoring point required by a joint friction model and structured such that only ordinary differential equations result, thereby permitting efficient computer implementation without requiring the solution of complex differential-algebraic equations.

Kinematic analysis of the two-body system was performed to relate the inertial frame accelerations of the helicopter body and castor assembly to the generalized coordinates and their first and second time derivatives.

The final acceleration-level kinematic equations are expressed in matrix form as

$$\begin{Bmatrix} A^g_{Hx} \\ A^g_{Hy} \\ \alpha_H \\ A^g_{Cx} \\ A^g_{Cy} \\ \alpha_C \end{Bmatrix} = \begin{bmatrix} 1 & 0 & 0 & 0 \\ 0 & 1 & 0 & 0 \\ 0 & 0 & 1 & 0 \\ 1 & 0 & B_{43} & B_{44} \\ 0 & 1 & B_{53} & B_{54} \\ 0 & 0 & 1 & 1 \end{bmatrix} \begin{Bmatrix} \ddot{q}_1 \\ \ddot{q}_2 \\ \ddot{q}_3 \\ \ddot{q}_4 \end{Bmatrix} + \begin{Bmatrix} 0 \\ 0 \\ 0 \\ C_4 \\ C_5 \\ 0 \end{Bmatrix} \tag{1}$$

where

$$B_{43} = -R^h_{\mathrm{B/H}_x} s q_3 - R^h_{\mathrm{B/H}_y} c q_3 + R^c_{\mathrm{B/C}_x} s(q_3 + q_4) + R^c_{\mathrm{B/C}_y} c(q_3 + q_4)$$

$$B_{44} = R^c_{\mathrm{B/C}_x} s(q_3 + q_4) + R^c_{\mathrm{B/C}_y} c(q_3 + q_4)$$

$$B_{53} = R^h_{\mathrm{B/H}_x} c q_3 - R^h_{\mathrm{B/H}_y} s q_3 - R^c_{\mathrm{B/C}_x} c(q_3 + q_4) + R^c_{\mathrm{B/C}_y} s(q_3 + q_4)$$

$$B_{54} = -R^c_{\mathrm{B/C}_x} c(q_3 + q_4) + R^c_{\mathrm{B/C}_y} s(q_3 + q_4)$$

$$C_4 = -R^h_{\mathrm{B/H}_x} c q_3 \dot{q}_3^2 + R^h_{\mathrm{B/H}_y} s q_3 \dot{q}_3^2 + R^c_{\mathrm{B/C}_x} c(q_3 + q_4)(\dot{q}_3 + \dot{q}_4)^2 - R^c_{\mathrm{B/C}_y} s(q_3 + q_4)(\dot{q}_3 + \dot{q}_4)^2$$

$$C_5 = -R^h_{\mathrm{B/H}_x} s q_3 \dot{q}_3^2 - R^h_{\mathrm{B/H}_y} c q_3 \dot{q}_3^2 + R^c_{\mathrm{B/C}_x} s(q_3 + q_4)(\dot{q}_3 + \dot{q}_4)^2 + R^c_{\mathrm{B/C}_y} c(q_3 + q_4)(\dot{q}_3 + \dot{q}_4)^2$$

and where c and s represent cosine and sine functions, respectively. For subsequent analysis, Eq. (1) is written more compactly as

$$\{A\} = [B]\{\ddot{q}\} + \{C\} \tag{2}$$

where matrices and vectors are identified by comparison with Eq. (1).

Free-body diagrams for the helicopter and castor assembly bodies are shown in Fig. 3, where all of the applicable forces and moments acting on each body are indicated. Newton–Euler force and moment

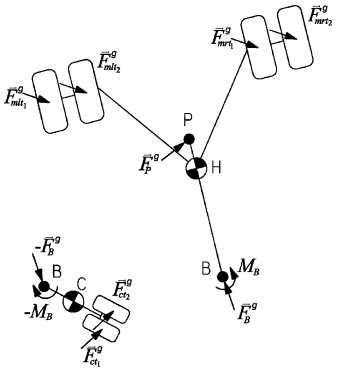

Fig. 3 Free-body diagram of the main helicopter body and castorable wheel assembly.

balance equations can be expressed in matrix form as

$$\begin{bmatrix} m_H & 0 & 0 & 0 & 0 & 0 \\ 0 & m_H & 0 & 0 & 0 & 0 \\ 0 & 0 & I_H & 0 & 0 & 0 \\ 0 & 0 & 0 & m_C & 0 & 0 \\ 0 & 0 & 0 & 0 & m_C & 0 \\ 0 & 0 & 0 & 0 & 0 & I_C \end{bmatrix} \begin{Bmatrix} A^g_{Hx} \\ A^g_{Hy} \\ \alpha_H \\ A^g_{Cx} \\ A^g_{Cy} \\ \alpha_C \end{Bmatrix}$$

$$= \begin{Bmatrix} F_1 \\ F_2 \\ F_3 \\ -F^g_{B_x} + F^g_{\mathrm{ct}_{x1}} + F^g_{\mathrm{ct}_{x2}} \\ -F^g_{B_y} + F^g_{\mathrm{ct}_{y1}} + F^g_{\mathrm{ct}_{y2}} \\ F_4 \end{Bmatrix} \tag{3}$$

where

$$F_1 = F^g_{P_x} + F^g_{\mathrm{dx}_x} + F^g_{\mathrm{dy}_x} + F^g_{B_x} + F^g_{\mathrm{mlt}_{x1}} + F^g_{\mathrm{mlt}_{x2}} + F^g_{\mathrm{mrt}_{x1}} + F^g_{\mathrm{mrt}_{x2}}$$

$$F_2 = F^g_{P_y} + F^g_{\mathrm{dx}_y} + F^g_{\mathrm{dy}_y} + F^g_{B_y} + F^g_{\mathrm{mlt}_{y1}} + F^g_{\mathrm{mlt}_{y2}} + F^g_{\mathrm{mrt}_{y1}} + F^g_{\mathrm{mrt}_{y2}}$$

$$F_3 = \boldsymbol{R}^g_{\mathrm{P/H}} \times \boldsymbol{F}^g_P + \boldsymbol{R}^g_{\mathrm{B/H}} \times \boldsymbol{F}^g_B + \boldsymbol{R}^g_{\mathrm{mlt/H_1}} \times \boldsymbol{F}^g_{\mathrm{mlt}_1} + \boldsymbol{R}^g_{\mathrm{mlt/H_2}} \times \boldsymbol{F}^g_{\mathrm{mlt}_2}$$
$$+ \boldsymbol{R}^g_{\mathrm{mrt/H_1}} \times \boldsymbol{F}^g_{\mathrm{mrt}_1} + \boldsymbol{R}^g_{\mathrm{mrt/H_2}} \times \boldsymbol{F}^g_{\mathrm{mrt}_2} + \boldsymbol{R}^g_{\mathrm{CPx/H}} \times \boldsymbol{F}^g_{\mathrm{dx}}$$
$$+ \boldsymbol{R}^g_{\mathrm{CPy/H}} \times \boldsymbol{F}^g_{\mathrm{dy}} + M_B$$

$$F_4 = \boldsymbol{R}^g_{\mathrm{B/C}} \times -\boldsymbol{F}^g_B + \boldsymbol{R}^g_{\mathrm{ct/C_1}} \times \boldsymbol{F}^g_{\mathrm{ct}_1} + \boldsymbol{R}^g_{\mathrm{ct/C_2}} \times \boldsymbol{F}^g_{\mathrm{ct}_2} - M_B$$

For subsequent analysis, Eq. (3) can be written more compactly as

$$[M]\{A\} = \{F\} \tag{4}$$

where matrices and vectors are identified by comparison with Eq. (3).

Next, the kinematic analysis is combined with the dynamic analysis to obtain the general equations of motion for the helicopter. Substituting Eq. (2) into Eq. (4) and rearranging, such that the generalized accelerations are isolated on the left, leads to

$$[M][B]\{\ddot{q}\} = \{F\} - [M]\{C\} \tag{5}$$

At this point there are six equations with six unknowns: the second time derivatives of the four state variables and the two components of the reaction force acting on the castor joint. The unknown reaction force components $\{F_u\}$ are separated from the known forces $\{F_k\}$ such that

$$(F) = \{F_k\} + \{F_u\} \tag{6}$$

Equation (6) is substituted back into Eq. (5), and $\{F_u\}$ is placed on the left-hand side as follows:

$$[M][B]\{\ddot{q}\} - \{F_u\} = \{F_k\} - [M]\{C\} \tag{7}$$

The unknown forces are next extracted from the moment expressions using

$$\{F_u\} = [D] \begin{Bmatrix} F^g_{B_x} \\ F^g_{B_y} \end{Bmatrix} \tag{8}$$

where

$$[D] = \begin{bmatrix} 1 & 0 \\ 0 & 1 \\ -R^g_{\mathrm{B/H}_y} & R^g_{\mathrm{B/H}_x} \\ -1 & 0 \\ 0 & -1 \\ R^g_{\mathrm{B/C}_y} & -R^g_{\mathrm{B/C}_x} \end{bmatrix} \tag{9}$$

The matrices are merged to isolate all six unknowns on the left-hand side, resulting in a set of simultaneous linear equations that can be solved for the unknown accelerations and forces as follows:

$$[[M][B] - [D]] \begin{Bmatrix} \ddot{q}_1 \\ \ddot{q}_2 \\ \ddot{q}_3 \\ \ddot{q}_4 \\ F^g_{B_x} \\ F^g_{B_y} \end{Bmatrix} = \{F_k\} - [M]\{C\} \tag{10}$$

where the left-hand side coefficient matrix in Eq. (10) is given by

$$\begin{bmatrix} m_h & 0 & 0 & 0 & -1 & 0 \\ 0 & m_h & 0 & 0 & 0 & -1 \\ 0 & 0 & I_h & 0 & R^g_{\mathrm{B/H}_y} & -R^g_{\mathrm{B/H}_x} \\ m_c & 0 & m_c B_{43} & m_c B_{44} & 1 & 0 \\ 0 & m_c & m_c B_{53} & m_c B_{54} & 0 & 1 \\ 0 & 0 & I_c & I_c & -R^g_{\mathrm{B/C}_y} & R^g_{\mathrm{B/C}_x} \end{bmatrix}$$

and the right-hand side composite force vector is given by

$$\begin{Bmatrix} E_1 \\ E_2 \\ E_3 \\ F^g_{\mathrm{ct}_{x1}} + F^g_{\mathrm{ct}_{x2}} - m_c C_4 \\ F^g_{\mathrm{ct}_{y1}} + F^g_{\mathrm{ct}_{y2}} - m_c C_5 \\ \boldsymbol{R}^g_{\mathrm{ct/C_1}} \times \boldsymbol{F}^g_{\mathrm{ct}_1} + \boldsymbol{R}^g_{\mathrm{ct/C_2}} \times \boldsymbol{F}^g_{\mathrm{ct}_2} - M_B \end{Bmatrix}$$

where

$$E_1 = F^g_{P_x} + F^g_{\mathrm{dx}_x} + F^g_{\mathrm{dy}_x} + F^g_{\mathrm{mlt}_{x1}} + F^g_{\mathrm{mlt}_{x2}} + F^g_{\mathrm{mrt}_{x1}} + F^g_{\mathrm{mrt}_{x2}}$$

$$E_2 = F^g_{P_y} + F^g_{\mathrm{dx}_y} + F^g_{\mathrm{dy}_y} + F^g_{\mathrm{mlt}_{y1}} + F^g_{\mathrm{mlt}_{y2}} + F^g_{\mathrm{mrt}_{y1}} + F^g_{\mathrm{mrt}_{y2}}$$

$$E_3 = \boldsymbol{R}^g_{\mathrm{P/H}} \times \boldsymbol{F}^g_P + \boldsymbol{R}^g_{\mathrm{mlt/H_1}} \times \boldsymbol{F}^g_{\mathrm{mlt}_1} + \boldsymbol{R}^g_{\mathrm{mlt/H_2}} \times \boldsymbol{F}^g_{\mathrm{mlt}_2}$$
$$+ \boldsymbol{R}^g_{\mathrm{mrt/H_1}} \times \boldsymbol{F}^g_{\mathrm{mrt}_1} + \boldsymbol{R}^g_{\mathrm{mrt/H_2}} \times \boldsymbol{F}^g_{\mathrm{mrt}_2}$$
$$+ \boldsymbol{R}^g_{\mathrm{CPx/H}} \times \boldsymbol{F}^g_{\mathrm{dx}} + \boldsymbol{R}^g_{\mathrm{CPy/H}} \times \boldsymbol{F}^g_{\mathrm{dy}} + M_B$$

An analytical solution for Eq. (10) has been found.[35] However, the complexity and length of the resulting expressions for the unknown quantities suggest that a numerical solution of Eq. (10) is more efficient for real-time simulation than evaluating the analytical expressions.

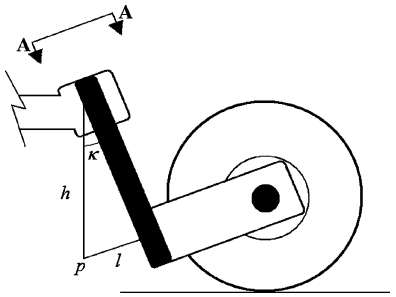

Fig. 4 Kingpin inclination angle.

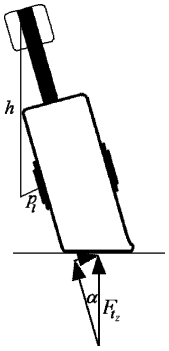

Fig. 5 Rotated castor wheel demonstrating the effect of the kingpin inclination angle.

2. Castor Joint Model

In the free-body diagram shown in Fig. 3, a reaction moment is shown at the pivot joint B. This moment is modeled using two torque contributions that include coulomb friction and viscous damping such that

$$M_B = T_\mu + T_\upsilon \tag{11}$$

Reaction force F_B at the castor pivot point is used to calculate the value of the coulomb friction at the castor joint using

$$T_\mu = -\text{sign}(\dot{q}_4)(\mu_B F_B r_\mu)\left(1 - e^{-\beta|\dot{q}_4|}\right) \tag{12}$$

The viscous damping component is proportional to the relative angular velocity of the castor assembly

$$T_\upsilon = C_B \dot{q}_4 r_\mu^2 \tag{13}$$

Some helicopter designs include a small inclination in the rotational axis of the castor joint as illustrated in Fig. 4. This is known as the kingpin inclination angle, and it creates an aligning torque to help align the castor assembly. A lateral force on the tires is created based on the rotation angle of the castor and the associated tendency to raise the helicopter. This lateral force is introduced to the dynamic equations as part of the force determined by the tire model. The straightening force is calculated using the normal force acting on the wheel and the geometry of the castor assembly, as shown in Figs. 5 and 6, resulting in

$$F_\kappa = -F_{t_z} \sin\kappa \sin q_4 \tag{14}$$

Detailed derivation of Eq. (14) is presented by Linn.[35]

Effectively locking the steerable or castorable wheel assembly at a particular orientation is accomplished by applying a torsional resistance with a very large stiffness and damping coefficient at the castor joint to oppose any motion. The castor joint moment, when the castor assembly is fixed, is calculated as

$$M_B = K_{\text{fix}} \delta q_4 + C_{\text{fix}} \dot{q}_4 \tag{15}$$

where δq_4 is the change in the rotational position of the castor assembly relative to a user-specified wheel angle.

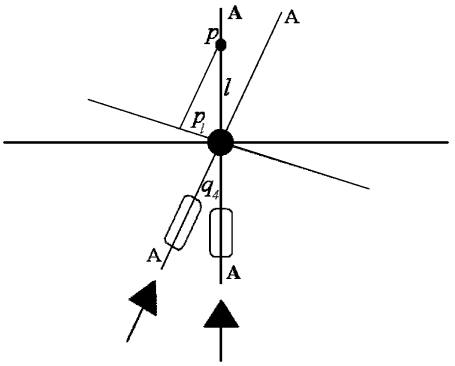

Fig. 6 AA view of the castor assembly.

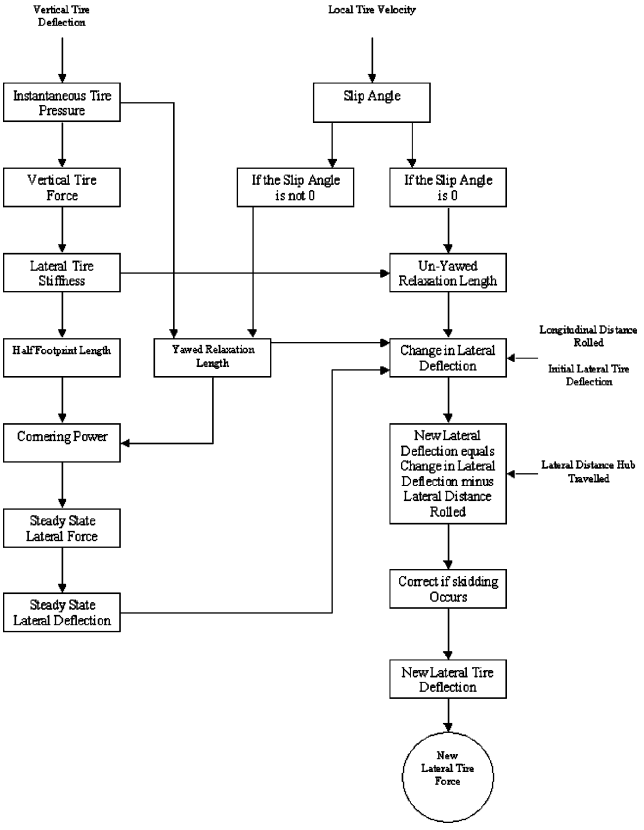

Fig. 7 Flowchart of the implemented tire model.

3. Tire Model

A three-degrees-of-freedom tire model has been constructed relying heavily on the empirical relationships presented by Smiley and Horne.[23] Figure 7 provides a flowchart overview of the structure of the tire model.

The following rolling resistance force model is applied in the tire's longitudinal direction.

$$F_{t_x}^t = \mu_{\text{rr}} F_{t_z}^t \left(1 - e^{-\beta|V_{t_x}^t|}\right) \tag{16}$$

This force opposes the wheel's velocity. A smoothing function has been applied to the rolling resistance [as was applied to the coulomb friction model in Eq. (12)] that prevents a force being applied when the wheel is not moving.

The lateral direction is more complex and involves calculating the generation and relaxation of lateral deflection. This is what creates the cornering force in the tire and is generated by the presence of a lateral tire velocity component as the tire is rolling. This lateral deflection relaxes when the tire rolls with no lateral velocity component. The rate at which the lateral deflection is generated or relaxed

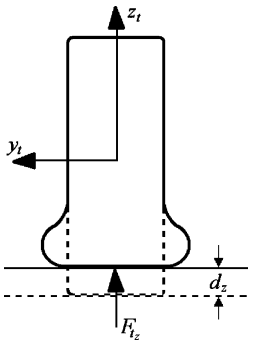

Fig. 8 Vertical tire deflection.

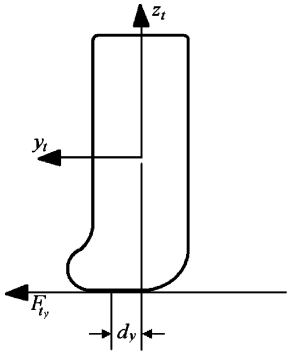

Fig. 9 Lateral tire deflection.

is based on the distance the tire must roll to reach a specific lateral deflection determined for the corresponding vertical tire loading.

The tire model relies on an iterative process to accurately capture the behavior. Each time the tire model is evaluated, new input conditions exist. These include the vertical tire deflection, local tire velocity, lateral and longitudinal distances the wheel hub has traveled, and the previous lateral tire deflection. In the planar simulation, all of these parameters change with the motion of the helicopter, except for the vertical tire deflection that is calculated once such that it is consistent with the helicopter weight distribution.

The instantaneous tire pressure is required to determine other parameters later in the model. Combining empirical relationships from Smiley and Horne[23] results in an expression for the instantaneous tire pressure as a function of vertical deflection:

$$P = P_0 + n(1.5w_t/2r_t)P_{0a}(d_z/w_t)^2 \tag{17}$$

It is assumed that the air compression process is isothermal with n being equal to 1. The instantaneous tire pressure is constant for the planar simulation.

Figure 8 illustrates exaggerated deflection caused by vertical loading. The empirical relationship between the vertical force and vertical deflection[23] states

$$F_{t_z} = [P + 0.08P_r]w_t\sqrt{w_t 2r_t}\, f_1(d_z/w_t) \tag{18}$$

where

$$f_1(d_z/w_t) = \left[0.96(d_z/w_t) + 0.216(d_z/w_t)^2\right]\Big/C_{\text{tz}} \quad \text{for} \quad d_z/w_t \le 10C_{\text{tz}}/3$$
$$f_1(d_z/w_t) = 2.4(d_z/w_t - C_{\text{tz}}) \quad \text{for} \quad d_z/w_t > 10C_{\text{tz}}/3 \tag{19}$$

Constant C_{tz} is equal to 0.02 for type I tires and 0.03 for types III and VII tires.

The lateral tire stiffness relates lateral tire force to lateral deflection as shown in Fig. 9. The lateral tire stiffness can be related to vertical tire deflection by the empirical relationship[23]

$$K_{t_y} = \tau w_t(P + 0.24P_r)[1 - 0.7d_z/w_t] \tag{20}$$

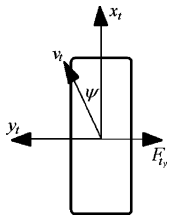

Fig. 10 Slip defined in the wheel reference frame.

where τ is 3 for type I tires and 2 for tire types III and VII. Lateral stiffness remains constant in the planar simulation.

The tire slip angle is defined as the angle between the direction the tire is pointing and the direction it is moving.[36] Figure 10 shows a positive slip angle and the direction of the resulting lateral force. The local tire velocity, which changes continuously, is used to calculate the slip angle ψ.

The unyawed relaxation length is defined as the distance the tire must roll in order for the lateral deformation to drop to a fraction $1/e$ of its initial value. Smiley and Horne[23] calculate this relaxation length as

$$L_u = (2.8 - 0.8P/P_r)(1.0 - 4.5d_z/2r_t)w_t \tag{21}$$

This length is used in Eq. (27) (presented subsequently) to calculate the change in lateral tire deflection during a relaxing phase.

The yawed relaxation length is defined as the distance the tire must roll in order to generate lateral tire deflection of $1/e$ times the difference between its initial value and the steady state value. Smiley and Horne[23] calculate this relaxation length L_y using the following equations based on $d_z/2r_t$:

For $d_z/2r_t \le 0.053$:

$$L_y = (11d_z/2r_t)(2.8 - 0.8P/P_r)w_t$$

For $0.053 > d_z/2r_t < 0.068$:

$$L_y = \left[64d_z/2r_t - 500(d_z/2r_t)^2 - 1.4045\right](2.8 - 0.8P/P_r)w_t$$

For $d_z/2r_t \ge 0.068$:

$$L_y = (0.9075 - 4d_z/2r_t)(2.8 - 0.8P/P_r)w_t \tag{22}$$

This length is used in Eq. (28) (presented subsequently) to calculate the change in lateral tire deflection during a force generation phase.

The cornering power represents the amount of lateral force the tire can generate for a given slip angle. It is used to calculate the steady-state lateral force

$$N = \left[L_y + 2r_t\sqrt{(d_z/r_t) - (d_z/r_t)^2}\right]K_{t_y} \tag{23}$$

The steady-state lateral force is the maximum lateral force that can be developed by a tire for a given slip angle. Following the introduction of a slip angle, a time lag will occur prior to the steady-state lateral force being reached. This steady-state lateral force is what is reached as the force is generated by the yawed relaxation. This steady-state lateral force is limited to the value at which sliding would initiate. The cornering power can be used to determine the steady-state lateral force according to the following relationships:

$$F_{\text{ss}_y} = \left(\mu F^t_{t_z}\right)(\phi - 4\phi^3/27) \quad \text{for} \quad \phi \le 1.5$$
$$F_{\text{ss}_y} = \mu F^t_{t_z} \quad \text{for} \quad \phi > 1.5 \tag{24}$$

where

$$\phi = \left(N\Big/\mu F^t_{t_z}\right)\psi \tag{25}$$

The steady-state lateral deflection can be calculated using the lateral tire stiffness

$$d_{\text{ss}_y} = F_{\text{ss}_y}/K_{t_y} \tag{26}$$

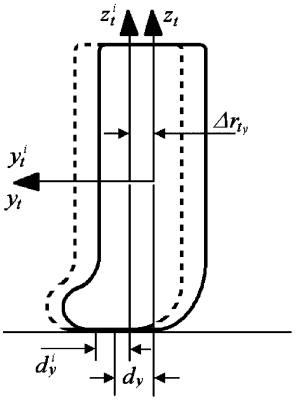

Fig. 11 Change in lateral tire deflection.

Once all of the tire parameters are determined, an intermediate lateral deflection can be calculated as a result of the unyawed or yawed relaxation length. Unyawed relaxation only occurs when the slip angle of the wheel is zero, resulting in

$$\Delta d_y = d_y^i e^{-|\Delta R_{t_x}^t|/L_u} \tag{27}$$

If the slip angle is nonzero, then yawed relaxation occurs, and the change in lateral deflection is calculated based on the empirical relationship

$$\Delta d_y = d_{ss_y} - \left(d_{ss_y} - d_y^i\right) e^{-|\Delta R_{t_x}^t|/L_y} \tag{28}$$

Next, the lateral distance the hub traveled in the previous time step must be considered, as shown in Fig. 11. This evaluates to

$$d_y = \Delta d_y - \Delta r_{t_y} \tag{29}$$

This therefore allows a lateral tire deflection to be developed as a result of side loading without the tire rolling forward.

Once the new lateral deflection is calculated, it must be tested against the maximum possible frictional force the tire and deck interface can support such that

$$K_{t_y} d_y > \mu F_{t_z}^t \tag{30}$$

If Eq. (30) is satisfied, the tire is sliding, and the value of d_y must be adjusted so the new lateral force equals the maximum allowable force based on the frictional sliding limit.

After the new lateral deflection is determined, the overall lateral force can be evaluated by considering the tire damping as well as the stiffness such that

$$F_{t_y}^t = K_{t_y} d_y + C_{t_y} \Delta V_{t_y}^t \tag{31}$$

The evaluated lateral and longitudinal tire forces are transformed into the global frame of reference and introduced into the governing dynamic equations.

4. RSD/Probe Model

The securing and handling system model initially simulated is based on the ITI ASIST system. Essentially, a controlled securing claw is moved longitudinally and laterally relative to the ship deck. The claw is interfaced to a helicopter-mounted resilient securing probe such that maneuvering forces are developed and transferred to the helicopter through the probe.

The RSD/probe model interprets input from the control model, described subsequently, and generates the forces that should be applied to the helicopter securing point. The deflection in the probe is used to generate the force. The physical operating limitations of the actual ASIST RSD system are imposed by the model.

Figure 12 shows a spring/damper representation of the probe that is used to determine the force acting on the probe. Langlois et al.[13] effectively use a bilinear spring for representing the probe stiffness. This permits representing a small amount of clearance between the

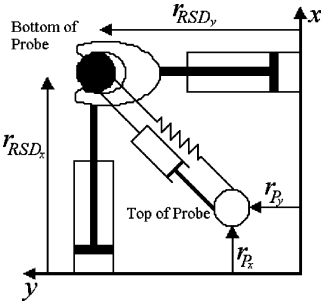

Fig. 12 Schematic of RSD/probe model showing the spring/damper representation of the probe.

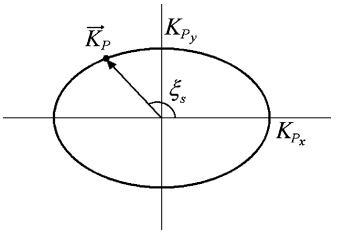

Fig. 13 Stiffness ellipse for the large deflection stiffness K_P^{eff}.

probe and the RSD claw. The contribution to the probe force as a result of the probe stiffness can be evaluated using the following:

For $|\boldsymbol{R}_{\mathrm{RSD/P}}| \le D_{\mathrm{Ps}}^{eff}$:

$$|\boldsymbol{F}_s| = |\boldsymbol{R}_{\mathrm{RSD/P}}| K_{\mathrm{Ps}}^{eff}$$

For $|\boldsymbol{R}_{\mathrm{RSD/P}}| > D_{\mathrm{Ps}}^{eff}$:

$$|\boldsymbol{F}_s| = D_{\mathrm{Ps}}^{eff} K_{\mathrm{Ps}}^{eff} + \left(|\boldsymbol{R}_{\mathrm{RSD/P}}| - D_{\mathrm{Ps}}^{eff}\right) K_P^{eff} \tag{32}$$

The magnitude and direction of the deflection are determined as follows:

$$|\boldsymbol{R}_{\mathrm{RSD/P}}| = \sqrt{\left(R_{\mathrm{RSD}_x}^g - R_{P_x}^g\right)^2 + \left(R_{\mathrm{RSD}_y}^g - R_{P_y}^g\right)^2} \tag{33}$$

and

$$\xi_s = \arctan\left(\frac{R_{\mathrm{RSD}_y}^g - R_{P_y}^g}{R_{\mathrm{RSD}_x}^g - R_{P_x}^g}\right) \tag{34}$$

The direction ξ_s is also the direction for the force $\boldsymbol{F}_s$.

A stiffness ellipse, as illustrated in Fig. 13 for the large deflection stiffness K_P^{eff}, has been applied to allow specifying different parameter values in the global x and y directions. The direction of the probe deflection determines the effective stiffness as the magnitude of the vector from the origin to the ellipse periphery. As an example, the large deflection stiffness is calculated using

$$K_P^{eff} = 1 \Big/ \sqrt{\left(\cos^2 \xi_s / K_{P_x}\right)^2 + \left(\sin^2 \xi_s / K_{P_y}\right)^2} \tag{35}$$

Analogous expressions are used for the soft deflection stiffness and transition displacement.

A similar procedure is applied for determining the probe viscous damping force recognizing that the damping and stiffness force directions can differ.

The stiffness and damping forces are combined to obtain the total force acting on the probe in the global frame of reference

$$\boldsymbol{F}_P^g = \boldsymbol{F}_s^g + \boldsymbol{F}_c^g \tag{36}$$

Once the probe force has been calculated, it is tested against the maximum applicable RSD force, and if it is above the limiting force the probe deflections are adjusted for the maximum force. Similar corrections are made with the RSD position limits. These limitations restrict the position of the RSD, and in effect the helicopter along with the forces that the RSD is able to apply to the probe. The maximum force the RSD can produce is determined by the pressure in the actual RSD hydraulic system.

5. Aerodynamic Model

An aerodynamic drag model is used to simulate aerodynamic forces acting on the helicopter. The general equation for determining the drag force is described by White[37] as

$$F_d = \tfrac{1}{2}\rho V_w^2 C_D A \tag{37}$$

Here the characteristic area is the profile area of the object perpendicular to the wind velocity, and the drag coefficient is based on the overall shape of the object.

The drag forces are calculated in the longitudinal direction using

$$F_{\mathrm{dx}}^h = \tfrac{1}{2}\rho V_{\mathrm{wx}}^h \left| V_{\mathrm{wx}}^h \right| A_{\mathrm{ex}} \tag{38}$$

and the lateral direction using

$$F_{\mathrm{dy}}^h = \tfrac{1}{2}\rho V_{\mathrm{wy}}^h \left| V_{\mathrm{wy}}^h \right| A_{\mathrm{ey}} \tag{39}$$

They are applied at the helicopter centers of pressure that can be different for each direction.

Both the wind velocity and ship velocity are considered when determining the drag forces. The maneuvering speed is insignificant compared with the apparent wind speed when significant aerodynamic forces occur and is therefore neglected.

B. Control Model

The control model allows three different methods for controlling the HeliMan simulation: tabulated input values can be read as the simulation is running; autonomous controller algorithms can be incorporated and evaluated; and an interactive joystick can be used to allow the user to maneuver the helicopter in real time using a simple graphical interface.

1. Joystick Input

The joystick input option mimics the joystick controller used in the actual ASIST system. A joystick position is used to specify a velocity to the RSD/Probe model. Figure 14 shows the velocity input profiles that the joystick applies based on its position. The X_J and Y_J axes specify the longitudinal and lateral RSD directions respectively. The lateral RSD direction is controlled by a simple on/off step function, while the longitudinal direction is controlled by a ramp function. Both directions also have a specific amount of deadband travel. Figure 14 shows a sample implementation appropriate for a control panel located starboard of the flight deck.

Two button functions are also available on the joystick. The first button models the float command. With the ASIST system, the operator has the option of letting the RSD float in a particular direction while it is moved in the direction perpendicular to the float direction. This essentially makes the applied force at the probe zero in the float direction by activating a pressure relief valve. If the float button is activated, the simulation relaxes the probe deflection by moving the RSD claw in the float direction and causing the force acting on the probe to be zero. The lateral float is implemented in

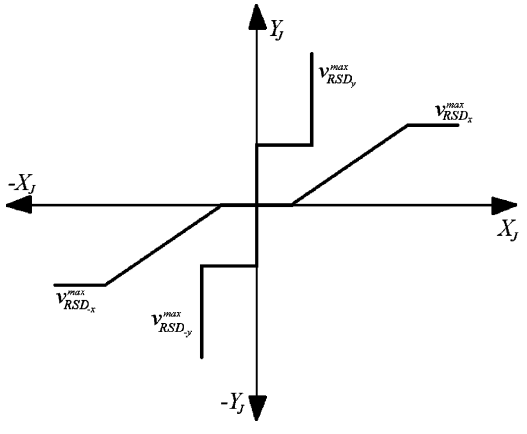

Fig. 14 Graph showing how the joystick specifies the RSD velocity.

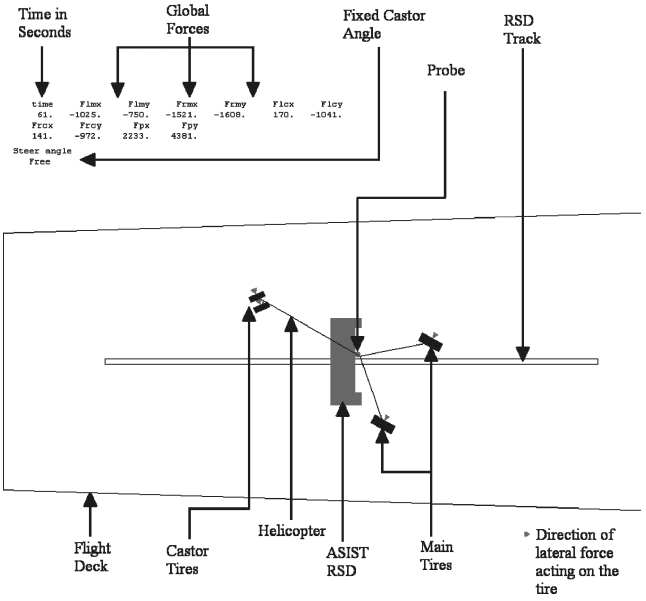

Fig. 15 Labeled HeliMan screen shot.

the joystick model as follows, noting that a lag coefficient prevents the float process from occurring instantaneously,

$$\mathrm{new}\dot{R}_{\mathrm{RSD}_y}^g = \dot{R}_{P_y}^g \tag{40}$$

$$\mathrm{new}R_{\mathrm{RSD}_y}^g = R_{\mathrm{RSD}_y}^g - \gamma_{\mathrm{lag}}\left(R_{\mathrm{RSD}_y}^g - R_{P_y}^g\right) \tag{41}$$

The second button specifies a steering angle option for the castor wheel in the simulation. Some helicopter types have steerable nose wheels that can be locked at specific steering angles. These predetermined steering angles are made available to the simulation in an input file. The button toggles through the steering angle options along with the free castor wheel option.

A graphics option is available to provide the HeliMan operator real-time feedback while controlling the RSD with the joystick. Figure 15 is an annotated screen shot of the graphical option available in HeliMan.

2. File Input

Alternatively, HeliMan can read input values from a file that has been generated using experimental results, hand calculations, or using HeliMan itself. In the latter case, input values are recorded in a file while the simulation is run in real time using the joystick. The simulation run can then be repeated using this file of input values. This feature is beneficial during validation and for analyses where repeating inputs exactly, which would be very difficult with a joystick, is necessary.

3. Controller Input

The controller input option uses parameters and state variables available within HeliMan to determine maneuvering command inputs. This control algorithm option determines and specifies RSD velocities using classical control methods. The nonlinear nature of the system does not lend itself to a traditional transfer function representation of controllers. Therefore, controller development must be done in the time domain using the simulation as the plant.

C. Simulation Model

The simulation model combines the various model elements. These include the equations of motion, tire model, RSD/probe model, castor joint model, aerodynamic model, and control model. Figure 16 illustrates how these parts are applied to the simulation process. All of the physical helicopter properties are input, along with the simulation parameters, which include the simulation time, initial position, and control profiles (if the joystick is not being used).

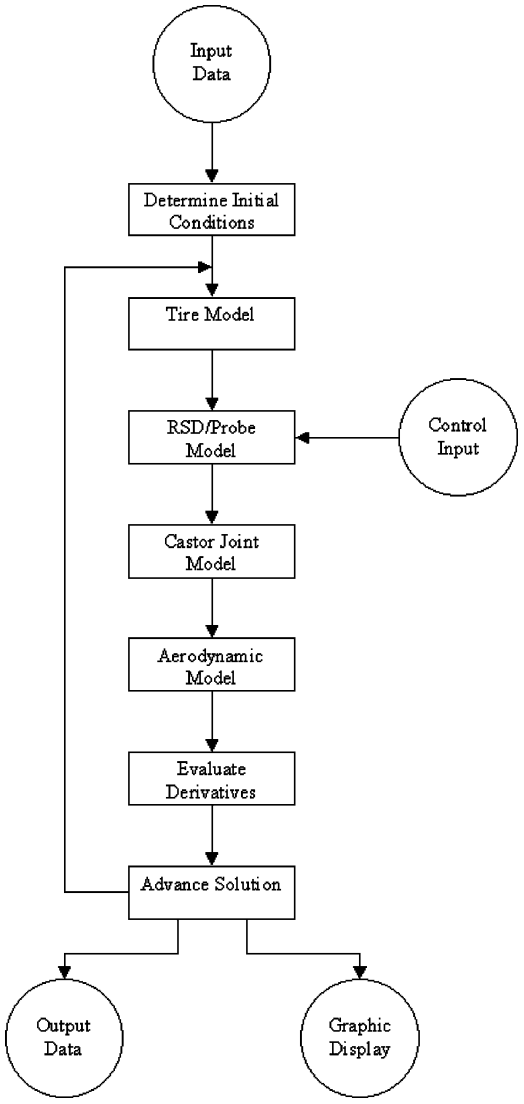

Fig. 16 Flowchart of HeliMan simulation.

Next, the initial forces and displacements are calculated based on the initial conditions specified by the user. Also at this point, all position vectors are transformed into the helicopter's frame of reference from the manufacturer's frame. The static load distribution on the tires is determined based on the specified aircraft weight and then used to calculate the vertical displacement of each tire. These vertical tire deflections are kept constant for the duration of the simulation run.

Once the initial conditions have been set up, the numerical integrator drives the solution forward in time, while obtaining control inputs from the joystick, input file, or internal calculations. A fixed-time-step fourth-order Runge–Kutta method has been found to meet numerical integration requirements.

As the simulation runs, information is gathered and output to a file for subsequent postprocessing and analysis. This information not only includes the output from the various models, but also can include an input file in the form of joystick inputs or probe forces as indicated previously.

III. Verification and Validation

The process of objectively evaluating the planar simulation, HeliMan, involved two stages: verification and validation. The verification stage was conducted to ensure that the mathematical model was implemented correctly in the simulation. The validation stage used experimental data to test how well the mathematical model represents the actual nonlinear system behavior.

Verification and validation were performed using helicopter parameters that are representative of a Sikorsky SH-60B Seahawk including a castoring tail wheel assembly with dual tires and single main tires.

A. Verification

For each model component, expected transition points were identified, and the simulation was run for parameters around the predetermined transitions. Model input and output data were extracted at representative key points, and the model results were compared with corresponding hand calculations. With the exception of the helicopter equations of motion, the models do not contain numerically integrated or time-dependent variables, but rather a series of equations that are exercised consistently at each time step. Consequently, verification at key points in the simulation was sufficient to ensure the models were implemented correctly. In all cases, exact agreement was obtained within the expected numerical precision, thereby confirming correct implementation of the various mathematical models.

B. Qualitative Validation

The joystick and graphical interface were used continuously during the development of HeliMan to validate the simulation qualitatively. Any significant discrepancies seen during the development process were addressed immediately. Experienced ASIST design engineers and operators tested HeliMan performance periodically and provided qualitative recommendations that were used to guide subsequent development.

C. Full-Scale Experimentation Validation

The final validation of HeliMan used data generated from full-scale experimentation on the ITI Integrated Test Facility (ITF).

The ITF, illustrated in Fig. 17, simulates the aft flight deck of a typical frigate. As with all naval vessels having helicopter facilities, the surface of the ITF is painted with antislip paint consistent with military standard MIL-D-23003. This allows for accurate representation of flight-deck characteristics. For simulation validation testing, the ITF was configured with an operational ASIST system and a full-scale dead load test vehicle (DLTV) representative of a Sikorsky SH-60B Seahawk helicopter. During testing, the following data were gathered from the ITF for each validation case considered: 1) longitudinal RSD claw velocity; 2) lateral RSD claw position; 3) longitudinal and lateral force components acting on the probe, measured in the helicopter frame of reference; 4) helicopter position measured manually at discrete times (used as a check for the first item); 5) helicopter orientation measured manually at discrete times; 6) lateral deflections of the main tires; and 7) castor wheel orientation up to ± 180 deg. The lateral deflections of the tail tires and an indication of when the float function was used were not recorded.

A wide range of test conditions was planned and executed on the ITF. These tests addressed the following: 1) quantifying the system lateral stiffness; 2) traversing while yawed with a fixed castor assembly orientation; 3) yawing to 90 deg from aligned; 4) yawing

Fig. 17 ITI's ITF and full-scale DLTV.

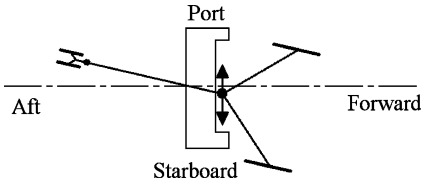

Fig. 18 Initial position of DLTV and direction RSD was moved for test case 1.

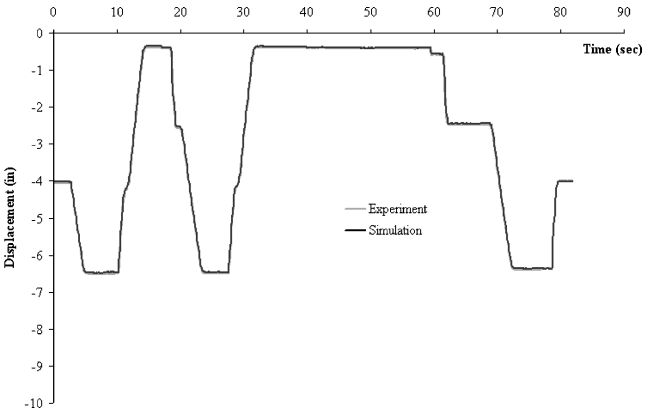

Fig. 19 Comparison of the RSD claw *y* position for case 1.

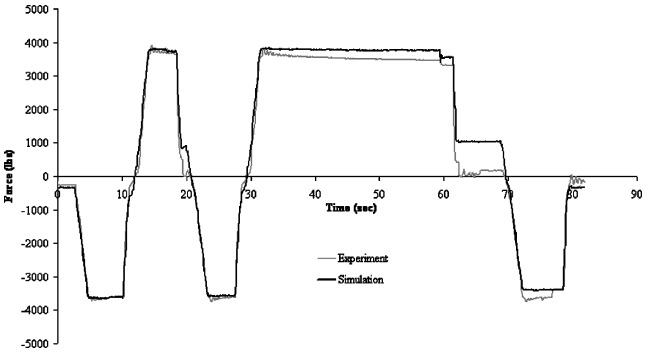

Fig. 20 Comparison of the force acting on the main probe in the DLTV's *y* direction for case 1.

back to aligned from 90 deg using free float; 5) rotating the castorable wheel by 180 deg; and 6) traversing with lateral tire deflections and a tail probe.

For case 1 the DLTV was located and oriented as shown in Fig. 18 with an initial orientation angle of 13 deg to starboard. The castor assembly was also locked in the aligned position. The purpose of this case was to test the lateral stiffness of the entire system. Once the DLTV was set up in its initial position, the operator moved the RSD claw laterally back and forth to build probe forces in the lateral direction. At the end of the test case, the operator used the float function to dissipate the accumulated force. This was done continuously as it was assumed that the longitudinal position of the RSD and the DLTV orientation would remain constant.

Figure 19 shows the measured and simulated lateral position of the RSD claw, and Fig. 20 shows the corresponding lateral probe force where the positive *y* axis is perpendicular to the DLTV longitudinal axis and directed positive to port. The displacement inputs to the simulation match exactly with the experimental data. The RSD claw started out 4 in. (10.2 cm) to the starboard side. Next, the operator manipulated the RSD claw back and forth in the lateral direction. At approximately 60 s the operator used the float function to dissipate the force that was built up. The RSD claw was then moved towards the starboard side, and the float function was used again. Some minor inconsistencies can be observed in the force plot (Fig. 20) when the float function was used.

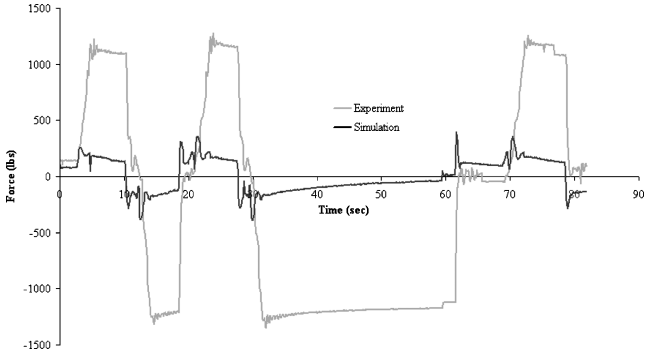

Fig. 21 Comparison of the force acting on the main probe in the DLTV's *x* direction for case 1.

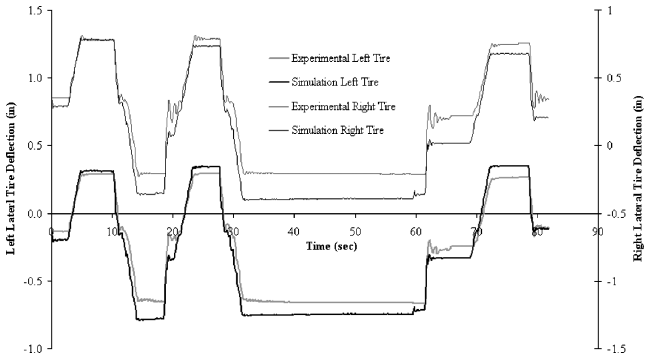

Fig. 22 Comparison of the lateral tire deflections for case 1.

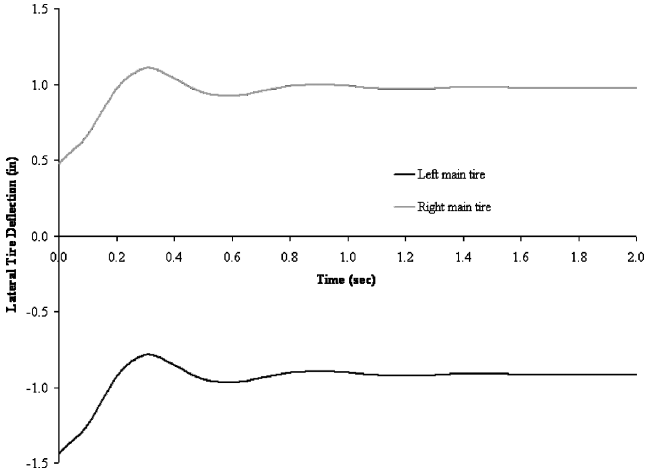

Fig. 23 Demonstration of the simulation's tendency to balance out the lateral tire deflections.

Oscillations in the experimental data were caused by the suspension on the DLTV. HeliMan does not currently model the suspension dynamics, and so the effect of any oscillations caused by the suspension does not appear in the simulated results.

Figure 21 shows the probe force in the DLTV *x* direction. A significant difference exists between the experimental data and that generated by the simulation. It was determined that the problem was caused by a shortcoming of the conventional longitudinal tire rolling resistance model. It is evident that lateral loading significantly affects the longitudinal frictional resistance.

Figure 22 shows plotted results for the lateral tire deflections for the main gear. Over the first few seconds, the lateral deflections generated by the simulation tend to balance out. This tendency is shown more clearly in Fig. 23. If the two main tires have opposite lateral deflections of significantly different magnitudes, the tendency of the system is to adjust the position of the helicopter body to balance the magnitudes.

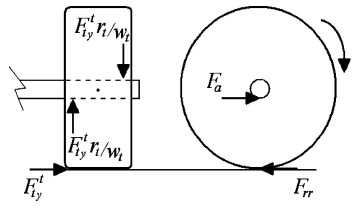

Fig. 24 Schematic of forces acting on the tire axle.

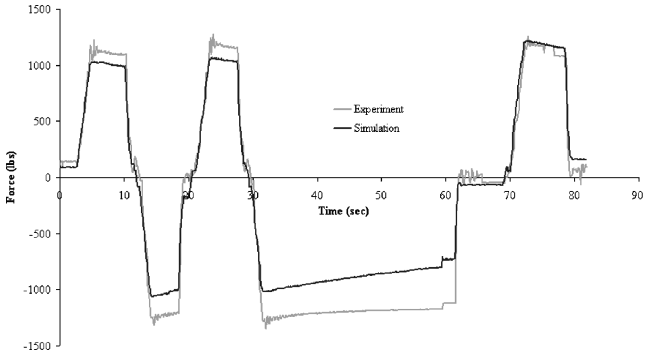

Fig. 25 Comparison of the force acting on the probe in the DLTV's *x* direction for case 1 with the new axle friction component.

This tendency causes the offset in the lateral deflections observed in Fig. 22. The experimental data did not show this tendency. This could be influenced by deflections of the castor tires, which were not recorded, counteracting the tendency to balance. The simulation was run under the assumption that the unmeasured lateral deflections of the castor tires were zero, which was almost certainly false.

A corrective component for the tire model was derived to address the problem with the main probe force in the x direction observed in Fig. 21. It was speculated that the lateral force acting on the tire causes a couple on the wheel axle that in turn increases the frictional resistance moment between the axle and the wheel and correspondingly an effective resistance force at the tire-ground interface. This force balance is shown in Fig. 24. The axle frictional force F_a was found to be

$$F_a = 2\mu_a(r_a/w_t)F_{t_y}^t \tag{42}$$

where the factor 2 results from the two point loads on the axle and μ_a is the coefficient of friction between the axle and the wheel. The magnitude of μ_a was selected to match the experimental data. Parameter r_a is the axle radius. The same μ_a and r_a parameters were used for the main and tail tires. The radius of the tire effectively cancels out.

The additional friction force was then added to the force acting on the tire in the longitudinal direction $F_{t_x}^t$. Further, a modified smoothing function was used to prevent the force from acting when the wheel is not rotating.

Figure 25 shows the revised simulation results for the main probe force in the x direction with the tire axle friction added. When compared to the simulation results presented earlier in Fig. 21, the added component has improved the accuracy of HeliMan significantly. The added component had no effect on the y component of the main probe force and the lateral tire deflections for case 1. Therefore, the revised simulation was used for case 2.

It was found in case 2 and early analysis of several subsequent cases that the added axle friction model did not improve the simulation performance and at some points increased the discrepancy between measured and simulated values. Further consideration leads to the observation that the axle friction force added to the simulation is a nonconservative force. This led to the conclusion that the longitudinal tire resistance force is governed by a more complex relationship than that presented by the combination of Eqs. (18) and (42) because of complex longitudinal and lateral tire behavior as well as axle tribology. The trend of the x component of the main probe force, for the experimental results, for the subsequent cases appears to be acting in a semiconservative manner. As a result, a more detailed longitudinal tire force model must be explored that includes tire elasticity in addition to the bearing friction component.

IV. Conclusions

The model presented has achieved the intended objectives of 1) developing a mathematical model that includes the helicopter equations of motion, the tires, the RSD/probe interface, and an optionally castorable auxiliary landing gear; 2) implementing the mathematical model in a real-time interactive computer simulation called HeliMan; and 3) analyzing the performance of the simulation using full-scale experimental data.

Of particular interest was the success of the formulation for the helicopter dynamics, which included the castor assembly body. The formulation allows reaction forces at the castor pivot joint to be determined and used to predict the coulomb friction acting at the castor joint.

The tire model was found to be the most complex aspect implemented in the simulation. The vertical and lateral stiffness models proposed by Smiley and Horne[23] were validated against data produced by the manufacturer of the tires on the DLTV though this tire validation only encompassed a portion of the entire tire model. During simulation validation, it was determined that the conventional rolling tire model fails to adequately capture apparent increases in longitudinal rolling resistance resulting from lateral wheel loading. The importance of this effect can be somewhat unique to this application where lateral tire loading is relatively high.

Although some limitations were found with HeliMan performance during the validation process, it predicted the position of the DLTV and the orientation of the DLTV and castor wheels reasonably well. The most significant limitation was found to originate in the implemented tire model. Refinement of the longitudinal rolling tire model is expected to remove this limitation.

The HeliMan simulation provides a versatile analytical tool that can be used to perform comprehensive on-deck helicopter maneuvering analysis. HeliMan currently provides the capability to simulate the basic behavior of the ASIST/helicopter system. HeliMan is currently applicable for the roles of qualitative demonstration of ASIST performance, operator training, and developing autonomous control algorithms. The proposed refinement of the tire model will be required for obtaining accurate quantitative results for detailed helicopter maneuvering analysis.

Acknowledgment

This project was sponsored jointly by Indal Technologies, Inc., where Atef Tadros was the technical authority; Materials and Manufacturing Ontario, where Carole Champion was the project liason, and Carleton University, where Rob Langlois was the principal investigator.

References

[1]Joelson, E. R., "Shipborne Helicopter—Landing, Security, Manoeuvring, and Traversing: Options and Implications," The Royal Institute of Naval Architects, Paper No. 15, London, June 1997.

[2]Carignan, S. J. R. P., Gubbels, A. W., and Ellis, K., "Assessment of Handling Qualities for the Shipborne Recovery Task—ADS 33 (Maritime)," American Helicopter Society, Vol. 56, May 2000, pp. 136–146.

[3]Zan, S. J., "Experimental Determination of Rotor Thrust in a Ship Airwake," *Journal of the American Helicopter Society*, Vol. 47, No. 2, 2002, pp. 100–108.

[4]Lee, R. G., and Zan, S. J., "Unsteady Aerodynamic Loads on a Helicopter Fusalage in a Ship Airwake," American Helicopter Society, Vol. 58, June 2002, pp. 10–21.

[5]McKillip, R. Jr., Boschitsch, A., Quackenbush, T., Keller, J., and Wachspress, D., "Dynamic Interface Simulation Using a Coupled Vortex-Based Ship Airwake and Rotor Wake Model," American Helicopter Society, Vol. 58, June 2002, pp. 1393–1424.

[6]Lee, D., Sezer-Uzol, N., Horn, J. F., and Long, L. N., "Simulation of Helicopter Shipboard Launch and Recovery with Time-Accurate Airwakes," American Helicopter Society, Vol. 59, May 2003, pp. 1113–1131.

[7]Aponso, B. L., and Jewell, W. F., "Rotorcraft Control Strategy in a Three-Dimensional Wind Shear Environment," American Helicopter Society, Vol. 58, June 2002, pp. 1463–1480.

[8]Keller, J. A., and Smith, E. C., "Analysis and Control of the Transient Shipboard Engagement Behavior of Rotor Systems," American Helicopter Society, Vol. 55, May 1999, pp. 1064–1079.

[9]Colwell, J. L., "Effects of Flight Deck Motion in High Seas on the Hovering Maritime Helicopter," American Helicopter Society, Vol. 58, June 2002, pp. 1489–1498.

[10]Bradley, R., and Turner, G., "Simulation of the Human Pilot Applied at the Helicopter/Ship Dynamic Interface," American Helicopter Society, Vol. 55, May 1999, pp. 677–688.

[11]Wei, F., Baitis, E., and Meyers, W., "Analytical Modeling of SH-2F Helicopter Shipboard Operation," *Journal of Aircraft*, Vol. 29, No. 5, 1992, pp. 877–885.

[12]de Smit, A., "CHSS-2/DDE Winch Down Securing Loads," United Aircraft of Canada Limited, Tech. Rept. H-1026, Montreal, Sept. 1966.

[13]Langlois, R. G., Sopher, G., and Tadros, A. R., *Aircraft/Ship Dynamic Interface Simulation: Dynaface, Release 5.0*, Indal Technologies, Inc., Mississauga, Ontario, Canada, 1999.

[14]Langlois, R. G., and Tadros, A. R., "State-of-the-Art on-Deck Dynamic Interface Analysis," American Helicopter Society, Vol. 55, May 1999, pp. 2111–2121.

[15]Langlois, R. G., and Tadros, A. R., "Parametric Investigation of the Sensititvity of Shipboard Helicopter Securing Requirements to Helicopter Configuration," *Proceedings of the Canadian Society for Mechanical Engineering Forum 2002*, edited by P. Oosthuizen, Paper No. 37, Queen's Univ., Kingston, Ontario, Canada, 2002.

[16]Langlois, R. G., LaRosa, M., and Tadros, A. R., "Development, Validation, and Application of the Dynaface Helicopter/Ship Dynamic Interface Simulation Software Package," *Proceedings of the SCSC 2003 Summer Computer Simulation Conference*, edited by V. W. Ingalls, Vol. 35, The Society for Modeling and Simulation International, San Diego, CA, 2003.

[17]Tadros, A. R., Langlois, R. G., and LaRosa, M., "Investigation of Ship Flight Deck Motion Limits for Safe Embarked Helicopter Operation," *Proceedings of the International Powered Lift Conference 2000*, American Helicopter Society, Paper No. 23, Alexandria, VA, 2000.

[18]Langlois, R. G., and Tadros, A. R., "Modelling the Aircraft/Ship Dynamic Interface," *Proceedings of the 16th Canadian Congress of Applied Mechanics*, edited by L. Cloutier and D. Rancourt, Vol. 1, Laval Univ., Quebec, Quebec, Canada, 1997.

[19]Kang, H., He, C., and Saberi, H., "Dynamic Interface Simulation of Rotorcraft Shipboard On-Deck Operation," American Helicopter Society, Vol. 59, May 2003, pp. 1080–1100.

[20]He, C., Kang, H., Carico, D., and Long, K., "Development of a Modeling and Simulation Tool for Rotorcraft/Ship Dynamic Interface Testing," American Helicopter Society, Vol. 58, June 2002, pp. 1425–1443.

[21]Xin, H., and He, C., "A Combined Technique for Inverse Simulation Applied to Rotorcraft Shipboard Operations," American Helicopter Society, Vol. 58, June 2002, pp. 1444–1462.

[22]Wall, A. S., Langlois, R. G., Zan, S. J., and Afagh, F. F., "Development of a Planar Model to Investigate the Effect of Ship Motion and Wind on Non-Rotating Helicopter Blade Flapping," *Proceedings of the Canadian Society for Mechanical Engineering Forum 2004*, edited by A. G. Straatman and B. E. Thompson, University of Western Ontario, London, Ontario, Canada, 2004, pp. 873–881.

[23]Smiley, R. F., and Horne, W. B., "Mechanical Properties of Pneumatic Tires with Special Reference to Modern Aircraft Tires," NASA TR-R-64, Jan. 1960.

[24]Zhou, J., Wong, J. Y., and Sharp, R. S., "Multi-Spoke, Three Plane Tyre Model for Simulation of Transient Behaviour," *Vehicle System Dynamics*, Vol. 31, No. 1, 1999, pp. 35–45.

[25]Zadeh, A. G., and Fahim, A., "An Analytical Transient Tire Model," *Tire Science and Technology*, Vol. 29, No. 2, 2001, pp. 108–132.

[26]Hashimoto, M., Yoshinaga, H., Yoshikawa, H., Morikawa, N., Uekusa, T., and Asai, S., "Three-Dimensional Finite Element Analysis of Loaded Tires," *NEC Research & Development*, Vol. 35, No. 4, 1994, pp. 477–487.

[27]Yu, H. J., and Aboutorabi, H., "Dynamics of Tire, Wheel, and Suspension Assembly," *Tire Science and Technology*, Vol. 29, No. 2, 2001, pp. 66–78.

[28]Shiraishi, M., Yoshinaga, H., Miyori, A., and Takahashi, E., "Simulation of Dynamically Rolling Tire," *Tire Science and Technology*, Vol. 28, No. 4, 2000, pp. 264–276.

[29]Hogg, C. R., "Simulation of Ground Handling of Taxiing Aircraft," Ph.D. Dissertation, Dept. of Mechanical and Manufacturing Engineering, Univ. of Brighton, Brighton, England, U.K., June 1993.

[30]Mallock, B., Harris, C. J., Hogg, C. R., and Jones, D., "Trimming of Flight Simulation Ground Models," *Proceedings of the Institution of Mechanical Engineers, Part G: Journal of Aerospace Engineering*, Vol. 211, No. 2, 1997, pp. 91–102.

[31]Self, A., Hogg, C., Pearce, D., and Kapadoukas, G., "The Simulation of Taxing and Low Flying Aircraft," *Proceedings of the 1992 EUROSIM Conference*, edited by F. Maceri and G. Iazeolla, North-Holland, Amsterdam, 1993, pp. 263–268.

[32]Kapadoukas, G. G., Self, A. W., and Harris, C. J., "Flight Simulation: Eigenvalue Analysis During Taxiing," *Proceedings of the Military, Government and Aerospace Simulation Conference*, edited by M. J. Chinni, Simulation Series, Vol. 26, The Society for Computer Simulation, San Diego, CA, 1994, pp. 121–126.

[33]Sleeper, R. K., and Smith, E. G., "A Transformation Method for Deriving, from a Photograph, Position and Heading of a Vehicle in a Plane," NASA-TN-D8201, May 1976.

[34]Sleeper, R. K., and Smith, E. G., "Planar Equations of Rollout Motion for an Aircraft with Free or Steerable Landing Gears," NASA-TP-1984, March 1982.

[35]Linn, D. R., "Development and Validation of a Planar on-Deck Helicopter Manoeuvring Simulation," M.A.Sc., Dept. of Mechanical and Aerospace Engineering, Carleton Univ., Ottawa, Ontario, Canada, Dec. 2003.

[36]Wong, J. Y., *Theory of Ground Vehicles*, 2nd ed., Wiley, New York, 1993, p. 29.

[37]White, F. M., *Fluid Mechanics*, 3rd ed., Schaums Outline Series in Mechanical Engineering, Schaum Div., McGraw–Hill, New York, 1994, Chap. 2.